Solid Earth, 14, 1067–1081, 2023
https://doi.org/10.5194/se-14-1067-2023

Solid Earth Open Access EGU

Glacial-isostatic-adjustment strain rate–stress paradox in the Western Alps and impact on active faults and seismicity

Juliette Grosset, Stéphane Mazzotti, and Philippe Vernant

Géosciences Montpellier, Université de Montpellier, CNRS, 34000 Montpellier, France

Correspondence: Juliette Grosset (juliette.grosset@umontpellier.fr)

Received: 22 March 2023 – Discussion started: 19 April 2023
Revised: 26 July 2023 – Accepted: 8 August 2023 – Published: 18 October 2023

Abstract. In many regions formerly glaciated during the Last Glacial Maximum (LGM), glacial isostatic adjustment (GIA) explains most of the measured uplift and deformation rates. GIA is also proposed as a key process contributing to fault activity and seismicity shortly after the LGM and potentially up to the present day. Here, we study the impact of GIA on present-day fault activity and seismicity in the Western Alps. We show that, in the upper crust, GIA induces horizontal compressive stress perturbations associated with horizontal extension rates. The latter agree with the observed geodetic strain rates and with the seismicity deformation patterns. Yet, in nearly all cases, the GIA stress perturbations tend to either inhibit fault slip or promote fault slip with the wrong mechanism compared to the seismicity deformation style. Thus, although GIA from the LGM explains a major part of the Western Alp geodetic strain rates, it does not drive or promote the observed seismicity (which must be driven by other processes). This apparent strain rate–stress paradox results from the gradual diminution over time of the finite shortening induced in the upper crust by the Würm ice cap load. A direct corollary of our results is that seismicity and seismic-hazard studies in the Western Alps cannot directly integrate geodetic velocities and strain rates but instead require detailed modeling of the GIA transient impact.

1 Introduction – glacial isostatic adjustment, deformation and seismicity

Glacial isostatic adjustment (GIA) is the mechanical response of the Earth's crust and mantle to loading–unloading cycles of continental ice sheets and glaciers. The associated surface deformation is observed in geomorphological features such as raised paleo-shorelines and in geodetic measurements of present-day uplift rates or horizontal strain rates (see review in Peltier et al., 2022). The impact of GIA and the associated stress perturbations on fault activity and seismicity has been studied since the seminal work of Johnston (1987), Quinlan (1984) and Stephansson (1988), up to recent developments including more complex Earth and fault mechanics models (see Steffen et al., 2021). A common feature of these studies is the demonstration that GIA increases fault activity and seismicity shortly after the main deglaciation phase in many regions formerly glaciated during the Last Glacial Maximum (LGM) (e.g., Wu et al., 1999; Stewart et al., 2000; Muir-Wood, 2000; Hetzel and Hampel, 2005; Steffen et al., 2014; Lund, 2015). In contrast, the potential effects of GIA stress perturbations on present-day faulting and seismicity in and near formerly glaciated regions remain debated (e.g., Bungum et al., 2010; Bungum and Eldholm, 2022; Brandes et al., 2015).

The first-order mechanics of GIA-related seismicity involves lithosphere flexure coupled with mantle relaxation in response to ice loading and unloading. Associated stress perturbations in the upper crust can reach a few megapascals, sufficient to induce rupture on faults near failure equilibrium or to unclamp faults, thus allowing the release of long-term stored tectonic stress (e.g., Craig et al., 2016; Hetzel and Hampel, 2005; Steffen et al., 2014). These effects are based on the same model (Fig. 1), wherein the ice loading results in a downward flexure and a horizontal compressive stress perturbation in the upper half of the elastic lithosphere beneath the load (upward flexure and extensive stress in the forebulge regions, respectively). Following deglaciation, the lithosphere unbending is dampened by the mantle viscosity, resulting in a gradual diminution of the initial bending stress.

The associated strain corresponds to a maximum shortening at the peak of glaciation followed by a diminution of shortening during the postglacial phase. As a result, the present-day surface strain rate corresponds to an extension rate, while the stress perturbation remains compressive. This apparent contradiction is similar to the strain rate–stress paradox observed in subduction zone forearcs in relation with transient interseismic locking of the megathrust fault (Wang, 2000). At the end of the GIA cycle, bending stress is fully released, and the plate regains its initial background state of stress (plus the potential steady-state tectonic loading) (Fig. 1).

Owing to GNSS (Global Navigation Satellite Network) data, present-day horizontal extension rates due to GIA have been measured with increasing accuracy not only in regions formerly covered by Wisconsin and Weichselian ice sheets (Calais et al., 2006; Keiding et al., 2015; Tarayoun et al., 2018), but also in regions of smaller ice caps and mountains glaciers, such as the Würm glaciation in the European Alps (Masson et al., 2019; Nguyen et al., 2016; Walpersdorf et al., 2018). These horizontal strain rates have been compared with seismicity deformation patterns and rates, with various degrees of agreement in both style and amplitude (Keiding et al., 2015; Mazzotti et al., 2005; Sánchez et al., 2018). One of the goals of these comparisons is the integration of GNSS velocities and strain rates in seismic-hazard models (Mathey et al., 2020), assuming that these short-term (5–20 years) data can provide information on longer-term (10^2–10^5 years) earthquake activity. However, the apparent GIA strain rate–stress paradox puts strong doubts on the pertinence of using GNSS rates to compare with seismicity in regions affected by ongoing transient GIA deformation (even more so for regions with very low tectonic loading rates such as intraplate domains).

In this study, we compare GIA deformation and stress predictions with present-day GNSS strain rates, fault activity and seismicity in the Western Alps (France, Italy, Switzerland), where GIA contributes to a large part of the measured geodetic deformation rates (Sternai et al., 2019; Stocchi et al., 2005). Specifically, we analyze the effect of GIA stress perturbations on a series of typical fault systems of the Western Alps in order (1) to compare with their observed kinematics and associated earthquake focal mechanisms and (2) to test whether GIA stresses tend to promote or inhibit the present-day seismicity.

2 Western Alp seismicity and GNSS strain rates

The Western Alps (Fig. 2) are one of the most seismically active regions in western Europe (Larroque et al., 2021). Background seismicity affects the whole region, with a high density of small to medium earthquakes ($M_w \geq 2.5$) in the high-altitude inner parts of the mountain range (Fig. 2b). In addition, several larger damaging earthquakes have occurred in the Western Alps over the last centuries (e.g., Epagny-Annecy, 1996: $M_w = 4.9$; Ligurian-Imperia, 1887: $M_w = 6.8$; Bale, 1356: $M_w = 6.5$). In the high-altitude inner areas, strain patterns derived from earthquake focal mechanisms show an overall normal-faulting style, with an extension direction perpendicular to the Alpine arc (Fig. 2b). These normal-faulting earthquakes can be divided into two clusters (oriented N–S): a western cluster, roughly in the Briançonnais region, with earthquake depths concentrated at ca. 5–10 km, and a smaller eastern cluster, with deeper focal depths of ca. 10–20 km (Mathey et al., 2021). The surrounding lower-altitude and foreland regions show a mix of strike-slip and reverse faulting with a general arc-perpendicular compression (Fig. 2b; Delacou et al., 2004; Mathey et al., 2021; Mazzotti et al., 2021; Sue et al., 1999). In general, only a few known fault structures can be associated with observed seismicity, e.g., the Belledonne Fault (Thouvenot et al., 2003), the Middle Durance Fault (Cushing et al., 2007) or the Vuache Fault (Baize et al., 2011). In contrast, most of the normal-faulting earthquakes in the inner massifs (above the Penninic Frontal Thrust) are not directly related to known major faults or structures (Larroque et al., 2021; Sue and Tricart, 2003).

The present-day geodynamics of the Central and Eastern Alps are primarily controlled by the counter-clockwise rotation of the Adriatic microplate relative to Eurasia, with a rotation pole east of the Western Alps near Turin, northwestern Italy (Fig. 2a; Battaglia et al., 2004; D'Agostino et al., 2008). However, this rotation kinematics are incompatible with the seismicity and geodetic horizontal deformation patterns horizontal deformation across the Western Alps is smaller than their current resolution, i.e., less than $0.3\,\mathrm{mm\,yr^{-1}}$ of relative motion between northwestern Italy (Po Plain) and the Rhône Valley, eastern France (Masson et al., 2019; Sánchez et al., 2018).

Geodetic data also indicate that the Western Alps are affected by a significant regional uplift rate between 0.5 and $2.5\,\mathrm{mm\,yr^{-1}}$, peaking in the inner high-altitude areas and decreasing towards $0\,\mathrm{mm\,yr^{-1}}$ in the surrounding lowlands (Fig. 3a; Brockmann et al., 2012; Masson et al., 2019; Nguyen et al., 2016; Nocquet et al., 2016). The highest uplift rates roughly coincide with horizontal arc-perpendicular extension rates of ca. $2 \times 10^{-9}\,\mathrm{yr^{-1}}$ in the inner regions (Switzerland, French–Italian border; Fig. 3b), while the surrounding lowlands show horizontal arc-perpendicular shortening rates of ca. $1\text{–}2 \times 10^{-9}\,\mathrm{yr^{-1}}$ (Jura, Rhône Valley; Fig. 3b) (Masson et al., 2019; Nguyen et al., 2016; Sánchez et al., 2018; Walpersdorf et al., 2018). The southern Western Alps are associated with a mix of extension and strike-slip rates of ca. $1\text{–}2 \times 10^{-9}\,\mathrm{yr^{-1}}$.

These strain rate amplitudes are at the limit of resolution of GNSS techniques and can only be identified through spatial low-pass filtering to remove short-wavelength noise. In a detailed analysis of real and synthetic data using a spatial Gaussian filter, Masson et al. (2019) show that a filter half-width of 70–100 km provides the best combination of spatial reso-

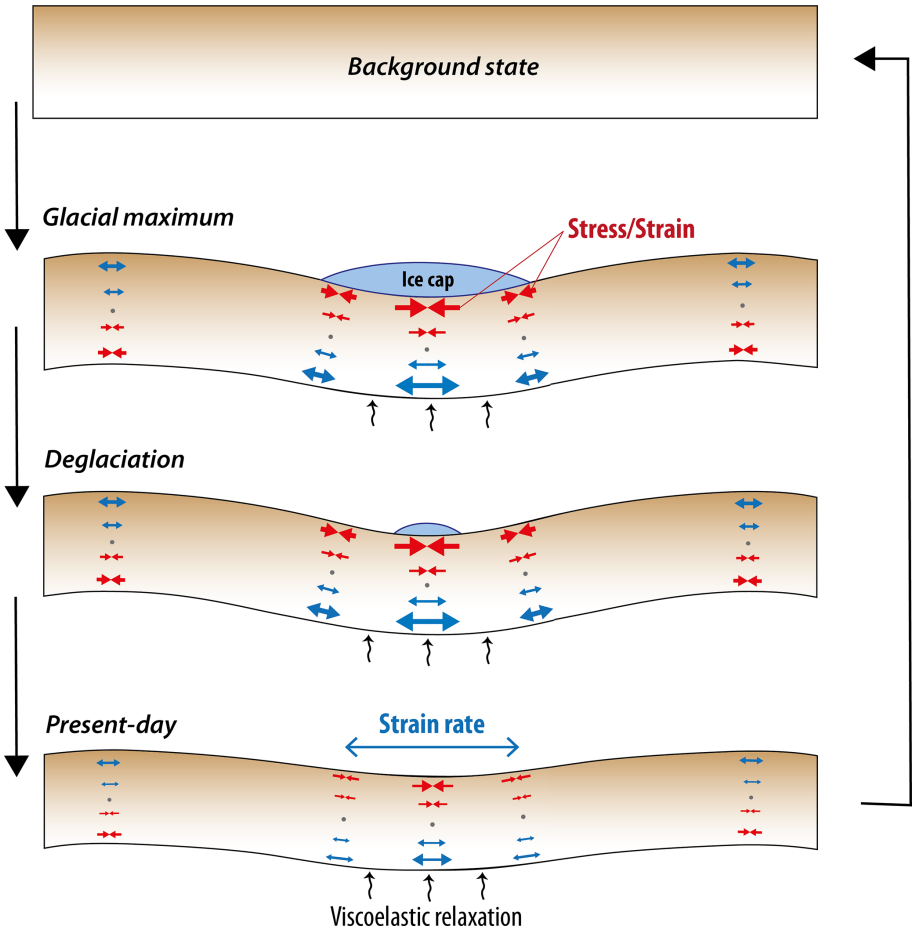

Figure 1. Conceptual model of glacial-isostatic-adjustment (GIA)-induced stresses, strains and strain rates.

lution and noise reduction for data in France and the Western Alps. This filter allows the identification of horizontal strain rate signals with a spatial coherence of ca. 100–200 km and a formal 95 % confidence interval of ca. 0.2–1.0 $\times 10^{-9}$ yr^{-1}, depending on the area, data quality and network geometry. Considering the dimensions of the Western Alps, their ice cap during the LGM and the lithosphere elastic thickness (see Sect. 3), 100–200 km is a reasonable estimation of the expected wavelength of the GIA signal. Thus, in the following, we apply the same 90 km half-width Gaussian filter to GNSS velocities and GIA model velocities for strain rate comparisons. Details of the method and additional strain rate maps at different filtering half-widths can be found in Sect. S1 in the Supplement for reference.

This overall deformation pattern (slow horizontal extension rates coupled with relatively fast uplift rates) is at the core of the current debate on the processes responsible for the ongoing geodynamics of the Western Alps. Because the role of regional plate tectonics is very small or null, recent studies consider alternative processes, including mantle and slab-tear dynamics (Sternai et al., 2019), surface erosion (Champagnac et al., 2007; Vernant et al., 2013), or GIA (Chéry et al., 2016; Mey et al., 2016). Numerical modeling shows that the isostatic response to erosion can generate the observed extension strain rate pattern, but the associated uplift rates are significantly smaller than the GNSS velocities (Sternai et al., 2019; Vernant et al., 2013). In contrast, GIA from the Last Glacial Maximum can explain the present-day uplift rates (Chéry et al., 2016; Mey et al., 2016), but a detailed comparison with horizontal deformation is lacking. In the following section, we test the compatibility of GIA models with present-day vertical and horizontal deformation rates of the Western Alps.

3 GIA models

3.1 Model setup

Due to the timescale of glacial loading–unloading cycles (10^2–10^5 years), GIA mechanical models consider both elastic and viscous deformation of the Earth's crust and mantle, with a large array of Earth rheology hypotheses and simplifications. In its simplest form, the surface response to GIA can be modeled as that of a thin elastic plate overlying a

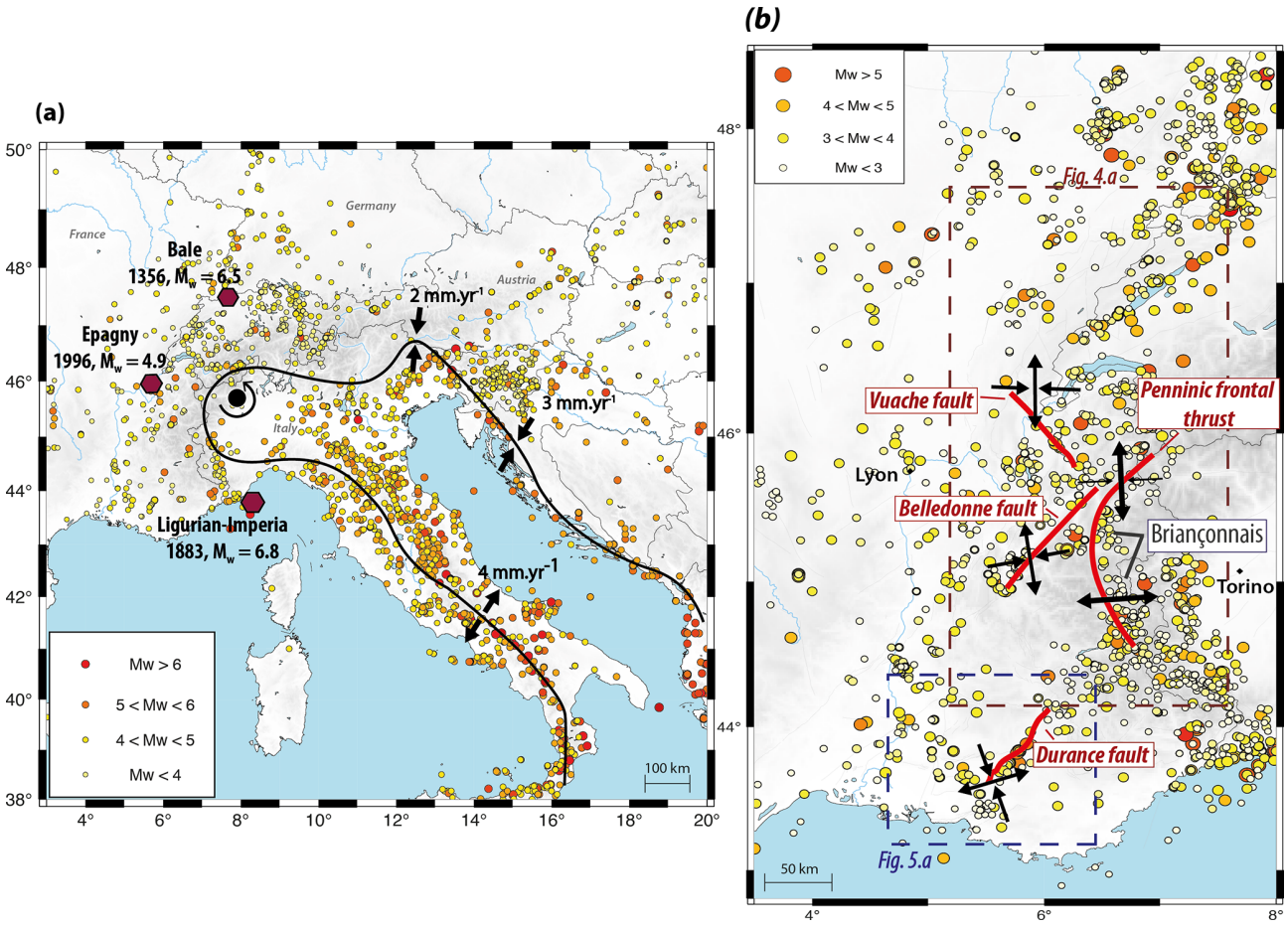

Figure 2. Western Alp tectonic and seismicity setting. **(a)** Instrumental seismicity of western Europe (catalogs: SHARE, Stucchi et al., 2013). Predicted Adriatic microplate motion relative to Eurasia represented along the Adriatic border. **(b)** Instrumental seismicity in the Western Alps (Manchuel et al., 2018) and interpreted seismic-strain styles from focal mechanisms (Rabin et al., 2018; Thouvenot et al., 1998, 2003; Cushing et al., 2008; Sue et al., 2003, 1999; Mathey et al., 2021).

linear viscous fluid (e.g., Mey et al., 2016). The more complex and most common modeling approach involves a 1D rheology stratification assuming an upper elastic layer, commonly 60–100 km thick, overlying multiple mantle layers with different Maxwell visco-elastic properties (see Peltier and Andrews, 1976; Spada et al., 2011). Higher levels of complexities can include asymmetrical 3D variations in rheology (elastic thickness and viscous properties; e.g., Bagge et al., 2021; Steffen et al., 2006; Wu, 2005), inclusion of viscous bodies within the elastic layer (e.g., Klemann and Wolf, 1999; Wu and Mazzotti, 2007), and non-linear or transient viscous rheologies (e.g., Giunchi and Spada, 2000; Lau et al., 2021; van der Wal et al., 2013).

Owing to the relative simplicity of both its parameterization and computation requirements, the 1D, symmetrical, Maxwell, layered model (hereafter "1D Maxwell") is the standard approach in most GIA studies. However, studies testing more complex rheology structures have shown that their predictions can deviate substantially from those of the 1D Maxwell model, with better fit to the surface observables in several cases (see Bagge et al., 2021; Lau et al., 2021; Steffen et al., 2006; van der Wal et al., 2013). Of particular note is the integration of non-linear transient mantle rheologies, which are also proposed to explain post-seismic relaxation following major earthquakes (e.g., Freed et al., 2010; Qiu et al., 2018). The integration of such time-dependent viscous rheologies in GIA models would imply significant biases in the standard 1D Maxwell viscosity estimations (Lau et al., 2021) but would also challenge the precept of stress advection/migration (Steffen et al., 2015; Wu, 1992), which directly results from the Maxwell body approximation for the Earth's mantle.

In this study, we consider the simplest form of GIA model predictions and use a thin elastic plate overlying a viscous substratum. The elastic plate flexure (w) in response to the ice load is computed using the Kirchhoff–Love thin-plate analytic solution (Turcotte and Schubert, 2002; Wickert, 2016), with a flexural rigidity defined by the plate thickness (h_e) and

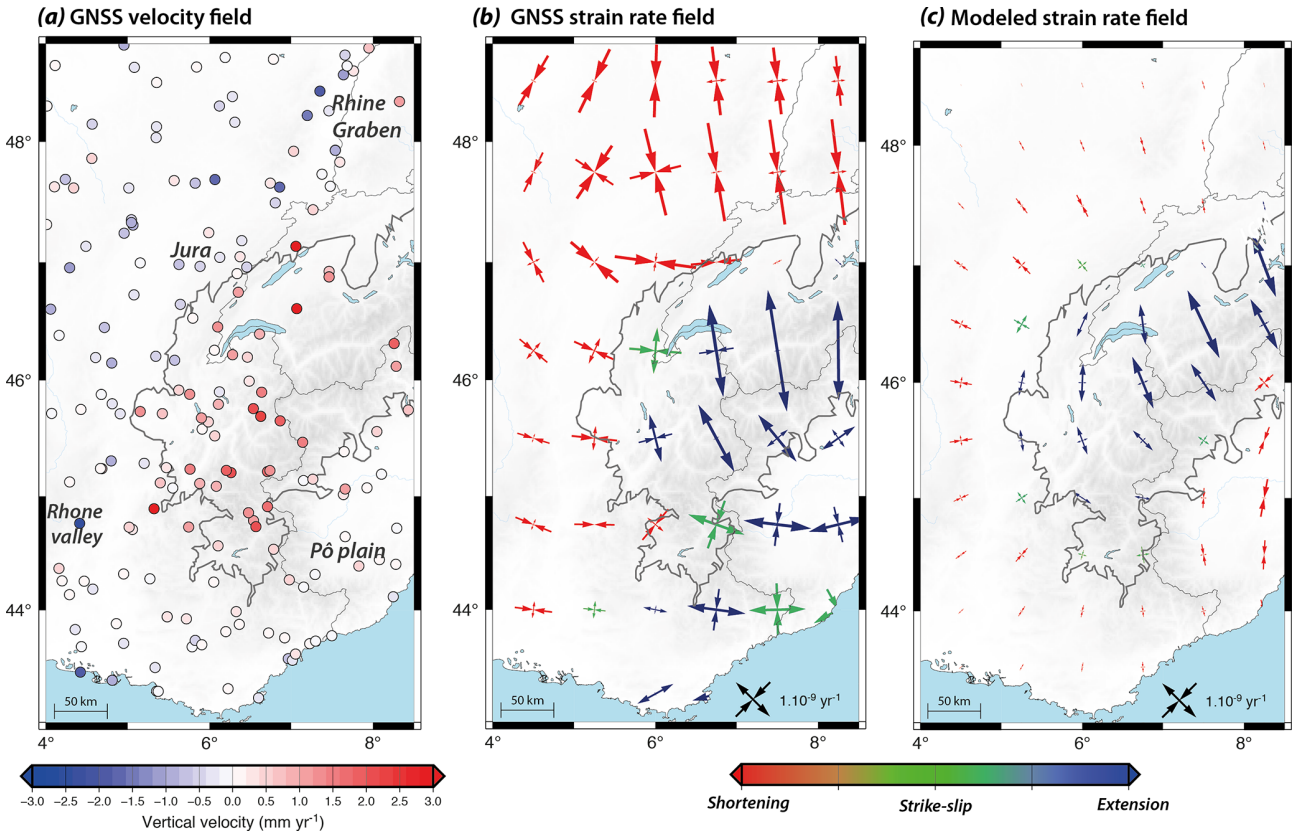

Figure 3. Western Alp geodetic and GIA deformation rates. **(a)** Vertical velocity field from permanent GNSS networks (Masson et al., 2019). **(b)** Horizontal strain rate field extracted from Gaussian filter method (see text). **(c)** Best-fit GIA model strain rate field ($h_e = 20$ km, $\tau_r = 5500$ years). Strain rates are color coded according to the deformation style. Gray line is Last Glacial Maximum ice extension (Mey et al., 2016).

its elastic parameters (Young modulus $E = 10^{11}$ Pa, Poisson coefficient $\nu = 0.25$). The elastic plate is laterally infinite. The flexure is computed from a superposition of analytical solutions (using gFlex code; Wickert, 2016). Bending strains and stresses in the elastic plate are computed from the second spatial derivative of the flexural response based on the Kirchhoff–Love theory (no vertical shear stress, only in-plane compression and tension stress). The time dependence of the response due to the upper-mantle viscous relaxation is computed assuming an exponential decay controlled by a relaxation time (τ_r):

$$w(x, y, t) = w(x, y)\, e^{-t/\tau_r}. \quad (1)$$

For the ice model, we use the ice cap reconstruction at the LGM from Mey et al. (2016) based on an ice-flow model constrained by geomorphological ice extent and thickness data. The ice model covers the whole Alps, with a mean (maximum) thickness at the LGM (ca. 21 kyr BP) of 415 m (2445 m). In the Western Alps, the main ice load is located in the major valleys, up to 1000–1500 m ice thickness. Additional smaller ice lobes (a few hundred meters) were located in the Jura. Keeping in line with the simple modeling approach, we assume (1) that the Alpine ice cap reached isostatic equilibrium at the LGM, owing to the relatively short relaxation time of the viscous mantle (ca. 5000 years; see Sect. 3.2), and (2) that there was an instantaneous deglaciation of the ice cap at 15 kyr BP, considering that 80 % melted between 21 and 18 kyr BP, and the remaining disappeared by 12 kyr (Ivy-Ochs et al., 2008).

Using this simplified approach is justified by several points. (1) We are only interested in the present-day state of stress and deformation to compare with seismicity and geodetic data. Time variations in GIA responses since the LGM are not relevant to our study, as long as they reach similar present-day states. (2) Alpine GIA models can only be constrained using present-day velocities and strain rates. Thus, the path leading to this present-day state (and thus the dependency on rheology assumptions) is unconstrained. (3) The Western Alp ice cap during the LGM has characteristic dimensions of a few hundred kilometers (Fig. 3). This relatively small load dimension only excites upper-mantle relaxation and is thus insensitive to deep-mantle rheologies (Steffen et al., 2015). (4) Small (few thousand years) time variations in the deglaciation history only impact our present-day

results by a few percent owing to the mantle relaxation time (see Sect. 3.2). These justifications for our simple approach are illustrated in the Supplement Sect. S2, in which we compare its results with those a standard 1D Maxwell model.

3.2 GIA velocities and strain rates

The analytical model allows testing of the sensitivity of predicted present-day GIA strain rates and stresses to the large range of assumed elastic plate rigidity and mantle relaxation time. Uplift rate predictions for models with a plate thickness $5 \leq h_e \leq 100$ km and a relaxation time $2000 \leq \tau_r \leq 20\,000$ years are compared with GNSS uplift rates (Fig. S5), assuming that the latter are largely due to GIA (Mey et al., 2016; Nocquet et al., 2016; Sternai et al., 2019). Using F-test statistics on these comparisons, we estimate a best-fit set of h_e and τ_r values to $h_e = 10$–20 km and $\tau_r = 4500$–5500 years. However, because present-day uplift rates may be impacted by other processes, in the following analysis we allow for a slightly larger range of values: $5 \leq h_e \leq 40$ km and $3000 \leq \tau_r \leq 7000$ years (in the following, computations and figures are presented for 72 GIA models with h_e and τ_r values distributed evenly within these ranges). These parameter values indicate a fast and short-wavelength response to the Last Glacial Maximum, in agreement with the results of more complex models (Chéry et al., 2016; Mey et al., 2016).

All retained models predict similar surface horizontal-strain-rate patterns, with N–S to NNW–SSE extension rates in the inner Western Alps (Figs. 3 and S6). These present-day extension rates are maximum in southwestern Switzerland and in the northeastern French Alps, reaching ca. 1–$2.5 \times 10^{-9}\,\mathrm{yr}^{-1}$. The forebulge regions (Rhône Valley, southern French Alps, eastern France) are associated with smaller shortening rates of ca. 0.2–$0.6 \times 10^{-9}\,\mathrm{yr}^{-1}$, with a shortening direction perpendicular to the Alpine arc. Transitional areas in between these extension and shortening domains show a variety of extension, strike-slip and shortening rates whose orientations and magnitudes vary strongly with the distance relative to the Würm ice cap and with the model parameters (Figs. 3 and S6). Thus, expected GIA strain rates in this narrow intermediate region are poorly defined.

To a first order, the GIA model strain rates are consistent with the horizontal strain rates derived from GNSS data in the inner parts of the northern Western Alps (Fig. 3b vs. 3c). In the Swiss–French border region, GIA model and GNSS strain rates agree in both orientation (with a small rotation from N–S to NNW–SSE) and in amplitude within their uncertainties (GIA model rates of ca. 0.9–$2.1 \times 10^{-9}\,\mathrm{yr}^{-1}$ vs. GNSS rates of ca. $2.5 \pm 0.5 \times 10^{-9}\,\mathrm{yr}^{-1}$). Similarly, in the French Alps GIA model rates are 0.4–$0.8 \times 10^{-9}\,\mathrm{yr}^{-1}$, in agreement with the GNSS rate of ca. $0.9 \pm 0.4 \times 10^{-9}\,\mathrm{yr}^{-1}$. We estimate that GIA accounts for a minimum of 30 % and up to 100 % of the GNSS extension rates observed in the inner Western Alps.

In contrast, the GIA models do not reproduce the relatively high GNSS E–W extension and strike-slip rates of ca. $1.5 \pm 0.5 \times 10^{-9}\,\mathrm{yr}^{-1}$ near the southern French–Italian border and in the western Po Plain (Fig. 3b vs. 3c). In this area, located directly south of the Adriatic–Eurasian rotation pole, the GNSS strain rates may be in part related to Adriatic microplate kinematics that would predict 0.3–$0.5\,\mathrm{mm\,yr}^{-1}$ of E–W extension in the southern Western Alps. Similarly, the GIA models do not explain the GNSS strain rates observed in the French and Swiss Jura and the southern Upper Rhine Graben. There, GIA model strain rates are consistent in style (shortening rates) and orientation with GNSS data, but their amplitudes are about 3–4 times smaller (Fig. 3b vs. 3c). This difference is too large to be explained by variations in the GIA model parameters (see Fig. S6), suggesting that the GNSS shortening rates cannot be solely attributed to Alpine GIA and that additional processes must contribute, such as possibly GIA effects from the Fennoscandian LGM ice sheets (e.g., Nocquet et al., 2005) or the deformation due to a mantle plume beneath the Eifel volcanic area (Kreemer et al., 2020).

4 Present-day GIA stresses, active faults and seismicity

4.1 GIA model vs. fault and seismicity depths

One of the main issues in using GIA models for studying stress perturbations on crustal faults is how the model setup relates to the actual Earth rheology and in particular its brittle and elastic domains. Although the upper elastic layer in GIA models is only a mechanical proxy for the crust and lithospheric-mantle flexural rigidity, all studies make the simple assumptions that (1) this elastic layer corresponds to the crust or lithosphere, depending on its thickness; (2) its top corresponds to the Earth surface; and (3) seismogenic faults are embedded in the elastic layer starting at its top (e.g., Hetzel and Hampel, 2005; Steffen et al., 2014). More complex models integrating elastic, brittle and ductile behaviors show that, under long-term geological loads, the lithosphere flexural rigidity resides where its resistance to failure exceeds ca. 10–20 MPa, which, in the upper crust, corresponds to depths below ca. 1–4 km (Burov and Diament, 1995; Hyndman et al., 2009; Tesauro et al., 2009). To our knowledge, no similar study exists for shorter-term loads like glaciation cycles. Thus, matching "real-Earth" depths, i.e., those of earthquakes or faults, with GIA model depths remains an issue.

In the Western Alps, most of the seismicity concentrates in the upper 10 km of the crust, except for the deeper cluster of extension seismicity at ca. 15–20 km depth east of the French–Italian border (see Sect. 2; Delacou et al., 2004; Mathey et al., 2021). In order to match our GIA model stress predictions to fault and seismicity depths, we consider the following points. (1) The range of GIA elastic plate thickness derived from GNSS data ($h_e = 10$–20 km; see Sect. 3)

corresponds primarily to the flexural rigidity of the crust. (2) The upper half of the elastic plate corresponds to a real-Earth depth range starting at ca. 1–4 km depth (see discussion above) and extending to ca. 6–14 km depth (starting depth plus half the plate thickness). (3) The lower half of the elastic plate extends from ca. 6–14 to ca. 11–24 km real-Earth depth. Thus, to a first order, the shallow (deep) seismicity level can be matched with the upper (lower) half of the GIA elastic plate. In the following, we use the maximum GIA stress perturbation derived at the top (bottom) of the elastic plate to discuss the impact on fault rupture, keeping in mind that the closer to the plate center, the smaller the GIA-induced stress perturbation.

4.2 Present-day GIA Coulomb-failure-stress perturbations

As expected from the conceptual flexural model (Fig. 1), shallow GIA stress perturbations correspond to horizontal compressive stresses below the former Alpine ice cap, including the present day (Fig. 4a), when uniaxial NNW–SSE compression of 2–3 MPa dominates in southern Switzerland up to the French and Italian borders, rotating to E–W compression of 1–2 MPa in the French Alps. These present-day shallow compressive horizontal stresses coincide directly with the region of current extension rates observed in the GNSS (compare Figs. 3b and 4a).

The impact of these stress perturbations on a given fault can be estimated using the variation in Coulomb failure stress (Δ_{CFS}) derived from the fault geometry and the associated fault shear and normal stress (King et al., 1994):

$$\Delta_{CFS} = \Delta\tau - \mu' \Delta\sigma_n, \quad (2)$$

with μ' the fault effective friction coefficient and $\Delta\tau$ and $\Delta\sigma_n$ the shear and normal stress perturbations on the fault. The fault-slip style associated with the stress perturbation is given by the rake (r) (Bott, 1959):

$$r = \arctan\left(\frac{\tau_d}{\tau_s}\right), \quad (3)$$

with τ_d and τ_s the shear stresses in the fault dip and azimuth directions, respectively.

In a first step, we consider the Coulomb-failure-stress perturbation to discuss the tendency of present-day GIA effects to promote slip ($\Delta_{CFS} > 0$) or inhibit slip ($\Delta_{CFS} < 0$) on a subset of fault systems in the Western Alps (a full Coulomb-failure-stress analysis integrating region stress regimes is discussed in Sect. 4.3). We consider three fault structures directly below the former ice cap (Fig. 4a): the Vuache Fault, the Belledonne Fault and a series of unknown faults associated with normal-faulting earthquakes in the Briançonnais directly east of the Penninic Front (hereafter IMNFs, inner-massif normal faults). The fault geometries are from neotectonic databases (Grellet et al., 1993; Jomard et al., 2017) or assuming Andersonian geometries for the unknown structures. Due to the fault dip uncertainties, we test a large range of dip angles (25–90°). Seismicity associated with these faults concentrates in the upper crust at ca. 5–10 km depth (Mathey et al., 2021; Thouvenot et al., 2003), associated with bending stresses in the upper half of the elastic plate (see Sect. 4.1).

Because the present-day GIA stress perturbations correspond to horizontal compressive stresses, faults with near-vertical dip angles (80–90°) and standard effective friction coefficients ($\mu' = 0.6$) tend to be clamped and are associated with negative Δ_{CFS} values (i.e., slip inhibition). In contrast, faults with low effective friction ($\mu' = 0.1$) or medium to low dip angles mostly show positive Δ_{CFS} between 0.1 and 2 MPa, indicating a tendency of GIA to promote fault slip in these cases. However, these models are associated with fault-slip rakes corresponding to mostly reverse faulting ($r = 50$–$130°$; Fig. 4b), opposite to that of earthquake normal-faulting mechanisms along the IMNFs ($r \approx -90°$; Fig. 4b; Mathey et al., 2021) and at odds with the strike-slip mechanisms on the Belledonne and Vuache Faults ($r \approx 180°$ and $r \approx 0°$, respectively; Fig. 4b; Rabin et al., 2018; Thouvenot et al., 2003). Thus, in all cases, the present-day GIA stress perturbations do not favor the observed seismicity on the main fault structures of the northern French Alps below the former Würm ice cap.

The impacts of GIA along and outside the Würm ice cap margin are more difficult to assess for two main reasons: present-day GIA stress perturbations are much smaller, and, mostly, they are strongly sensitive to the model parametrization (elastic plate thickness, rheology assumptions). As an example, we estimate the impact on the Middle Durance Fault, one of the best characterized active faults in the southern French Alps (Cushing et al., 2008). There, present-day GIA stress perturbations correspond to horizontal NE–SW tension ranging from ca. 0.3–0.7 MPa at the northern end of the fault to ca. 0.1–0.3 MPa at its southern end (Fig. 5a). Δ_{CFS} is systematically positive (for a low effective friction), but, due to bends in the fault segments, the range of predicted rakes is very large: along the northern section, GIA favors right-lateral strike-slip rakes, while favored rakes flip between right- and left-lateral along the central and southern sections (Fig. 5b). Focal mechanisms along the Middle Durance Fault correspond to an overall left-lateral kinematics (Cushing et al., 2008), indicating that the present-day GIA stress perturbations may favor or inhibit slip depending on the considered segment.

4.3 Present-day full Coulomb failure stress

The combination of GIA stress perturbations with the background stress field defines the full Coulomb failure stress (CFS) for any given fault:

$$CFS = \tau - \mu' \sigma_n, \quad (4)$$

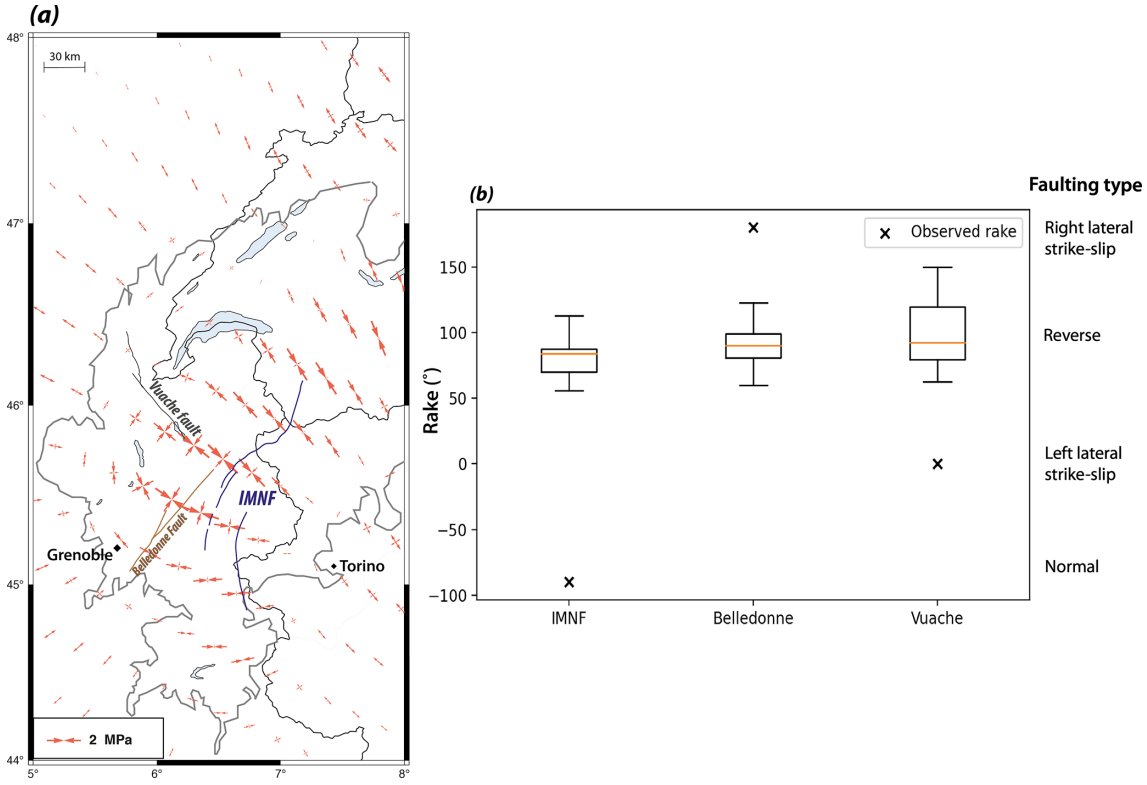

Figure 4. Present-day GIA stress perturbations and predicted fault-slip rakes in the northern Western Alps. **(a)** Horizontal GIA stress perturbations (model $h_e = 20$ km, $\tau_r = 5500$ years) and faults tested in the Coulomb-failure-stress perturbation analyses. **(b)** Fault-slip rakes predicted by GIA stress perturbations (boxplot) and observed from earthquake focal mechanisms (black cross; Billant et al., 2015; Delacou et al., 2004; Rabin et al., 2018; Sue et al., 1999; Thouvenot et al., 2003). Boxplots represent predictions for 72 GIA models distributed over an area of $5 \leq h_e \leq 40$ km over $3000 \leq \tau_r \leq 7000$ years, combined with three possible fault dips (IMNFs, inner-massif normal faults: 25, 45, 65°; Belledonne: 65, 70, 85°; Vuache: 60, 80, 80°). Orange lines: medians.

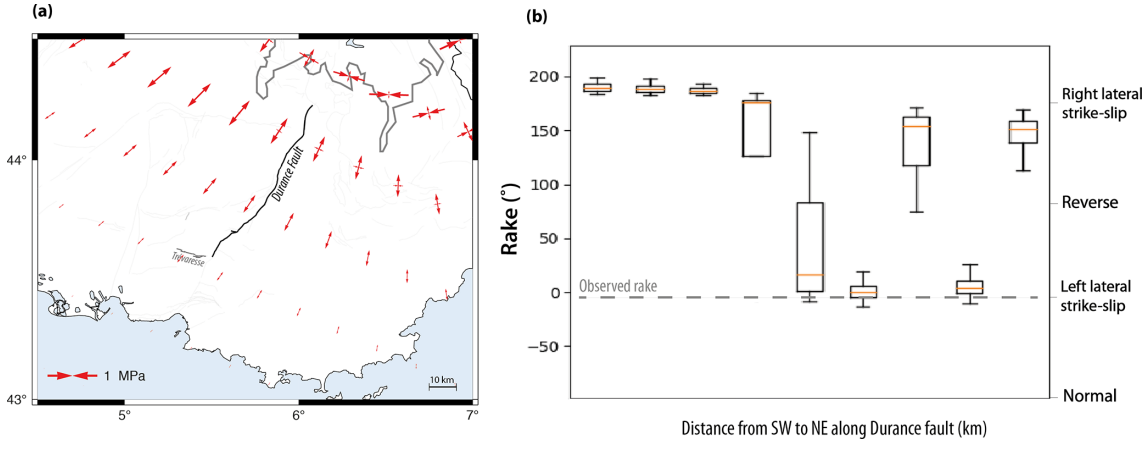

Figure 5. Present-day GIA stress perturbations and predicted fault-slip rakes in the southern Western Alps. **(a)** Horizontal GIA stress perturbations (model $h_e = 20$ km, $\tau_r = 5500$ years) and faults tested in the Coulomb-failure-stress perturbation analyses. **(b)** Fault-slip rakes predicted by GIA stress perturbations (boxplot) and observed from earthquake focal mechanisms (Cushing et al., 2008). Boxplots represent predictions for 72 GIA models distributed over an area of $5 \leq h_e \leq 40$ km over $3000 \leq \tau_r \leq 7000$ years, combined with three possible fault dips (60, 80, 85°). Orange lines: medians.

with τ and σ_n the shear and normal stresses acting on the fault, with the associated fault-slip rake given by Eq. (3). Depending on the geometric relationships between the stress perturbation, the background stress tensor and the fault geometry, the CFS indicates that a fault should (CFS >0) or should not (CFS <0) slip in the local deformation regime. A major difficulty in computing CFS is the definition of the background stress tensor. Given the lack of direct measurements at seismicity depths (5–20 km), this requires several assumptions that can strongly influence the CFS estimation. A second difficulty in the case of the Western Alps is the strong variations in the deformation and stress regimes over distances of tens of kilometers (Mathey et al., 2021; Delacou et al., 2004).

In order to test the conclusions drawn from the Δ_{CFS} analysis (Sect. 4.2), we compute the full CFS on two major fault systems representative of the central Western Alp present-day seismicity: the northern Briançonnais normal-faulting system (IMNFs) and the strike-slip Belledonne Fault (Fig. 2b). In each case, we construct a local background stress tensor using information from the focal-mechanism stress inversions of Mathey et al. (2021) and several additional assumptions for the IMNF and Belledonne systems:

- The deformation regime is pure normal faulting (IMNFs) or pure strike-slip faulting (Belledonne).
- The stress tensor is Andersonian, with the vertical stress (σ_V, lithostatic pressure) corresponding to σ_1 (IMNFs) or σ_2 (Belledonne).
- The azimuth of the maximum horizontal stress $\sigma_H = \sigma_2$ (IMNFs) or $\sigma_H = \sigma_1$ (Belledonne) is given by the focal-mechanism stress inversion.
- The differential stress ($\sigma_1 - \sigma_3$) is controlled by optimally oriented faults with an effective coefficient of friction μ' (Eq. 4) and following the Mohr–Coulomb friction law for a normal (IMNFs) or strike-slip (Belledonne) case (Jaeger and Cook, 1979).
- The shape of the stress tensor ($R = (\sigma_1 - \sigma_2)/(\sigma_1 - \sigma_3)$) is set to $R = 0.5$ (i.e., $\sigma_2 = 1/2\,(\sigma_1 + \sigma_3)$).
- The same coefficient of friction (μ') is used for the local background stress and the tested faults.

Results of the full CFS computation (local background stress + GIA perturbation) at 5 km depth for the northern Briançonnais extension system are summarized in Fig. 6. Assuming that the seismicity is associated with the reactivation of the Penninic Frontal Thrust (Bilau et al., 2021; Sue and Tricart, 1999), the variations in obliquity of the stress tensor to the fault geometry result in negative CFS from ca. -50 to -10 MPa for a standard friction $\mu' = 0.6$ (Fig. 6b). A small friction value $\mu' = 0.1$ results in smaller negative CFS (ca. -10 to 0 MPa). Relative to the modeled stress field, the northeastern section of the fault system is more favorably oriented than the southern section and shows the largest (less negative) CFS, up to CFS ≈ 0 MPa in the most favorable case ($\mu' = 0.1$, fault dip of 60°). In contrast, if we assume that the seismicity is associated with faults corresponding to the average focal mechanism (azimuth N050, dip 50°; Mathey et al., 2021), this fault geometry is close to optimal orientation relative to the stress tensor and yields small, mostly negative CFS (ca. -5 to $+1$ MPa; Fig. 6c). In a few specific cases, the GIA stress perturbation pushes the fault to small positive CFS <1 MPa. These cases correspond to models with a very thin elastic plate ($h_e \leq 10$ km) and a small friction value ($\mu' = 0.1$) on the southwestern fault section.

In nearly all cases, the GIA stress perturbations tend to diminish the CFS (render more negative) by a few megapascals, which confirms the tendency of present-day GIA to inhibit the normal-faulting seismicity in the Briançonnais region of the Western Alps. This is easily explained by considering that the GIA stress perturbations correspond to horizontal compressive stresses that tend to inhibit normal faulting (Sect. 4.2). A few specific cases can result in a positive effect of the GIA perturbation on CFS if the fault is nearly optimally oriented, and the GIA stress perturbation corresponds to a small subset of the tested parameter range.

The case of the Belledonne Fault system shows more variability (Fig. 7). The local background stress is associated with a σ_H azimuth of 107° N, strongly oblique to the strike of the Belledonne Fault. Thus, a standard friction $\mu' = 0.6$ yields large negative CFS (ca. -80 to -60 MPa at 5 km depth; Fig. 7b), whereas a small friction value $\mu' = 0.1$ brings the fault–stress configuration closer to an optimal geometry with smaller negative CFS (ca. -10 to -8 MPa; Fig. 7b). The impact of the GIA stress perturbations depends on the assumed fault friction, dip and position within the local stress field: for a standard friction $\mu' = 0.6$, the GIA perturbation systematically reduces the CFS, thus further inhibiting fault slip; for a small friction value $\mu' = 0.1$, the GIA perturbation can increase (render less negative) the CFS by 0.1–0.5 MPa if the fault dip is nearly vertical.

These two examples illustrate the complexity of full CFS estimations and their dependency on the fault and background stress parameters. Yet, their results generally confirm the main conclusion drawn from the Δ_{CFS} analysis (Sect. 4.2): the present-day GIA stress perturbation tends to inhibit fault slip for the extension and strike-slip systems of the central Western Alps (below the former ice cap). It is worth noting that because the GIA stress perturbations decrease exponentially with time, the crust will eventually return to its unperturbed (pre-GIA) normal and strike-slip stress regime, which should translate into a slow increase in seismicity in the Western Alps. A few specific configurations of background stress, fault geometry and fault friction can result in cases in which the GIA perturbation promotes fault slip. These particular configurations only apply to a very limited set of faults and earthquakes.

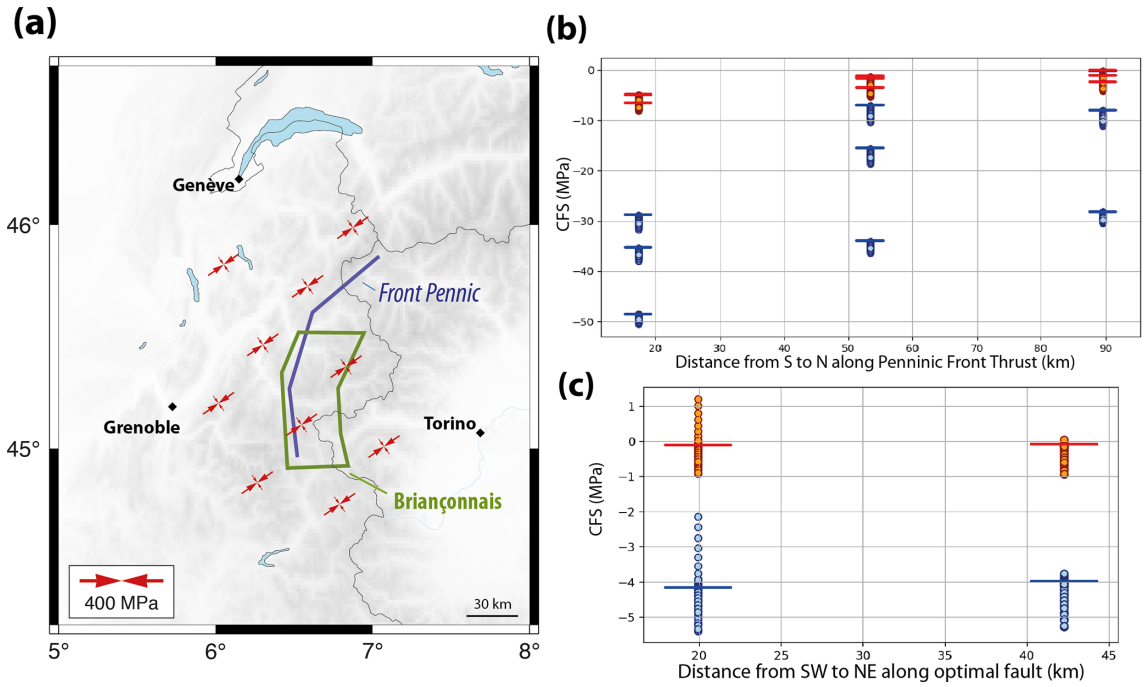

Figure 6. Present-day full stress tensor and Coulomb failure stress (CFS) for the Briançonnais shallow seismicity cluster in the northern Western Alps. **(a)** Horizontal full stress (background + GIA) and faults tested in the CFS analyses. **(b)** CFS predicted along the Penninic Front structure for three possible fault dips (30, 45, 60°) and 72 GIA models distributed over $5 \leq h_e \leq 40$ km over $3000 \leq \tau \leq 7000$ years. Horizontal bars: CFS without GIA perturbation for the three fault dips. **(c)** CFS predicted along optimally oriented fault structure in the Briançonnais area (dip = 50°) for 72 GIA models distributed over $5 \leq h_e \leq 40$ km over $3000 \leq \tau_r \leq 7000$ years. Horizontal bars: CFS without GIA perturbation for the three fault dips. Circles: full CFS (background + GIA). Blue and red symbols: $\mu' = 0.6$ and $\mu' = 0.1$.

The present analysis was carried out for a depth of 5 km, assuming that the GIA perturbation is maximum (i.e., top of the elastic plate; Sect. 4.1). A smaller GIA perturbation (i.e., deeper in the upper half of the elastic plate) and a deeper analysis depth would simply result in a smaller impact of the GIA on the full stress field and full CFS computations. The case of the deeper extension seismicity cluster (10–20 km depth) east of the Briançonnais cluster (see Sect. 2, Fig. 2b) is also worth noting, for which the GIA stress perturbation would be opposite to that at shallower depths (horizontal tension; Sect. 4.1) and would likely favor the normal-faulting seismicity.

5 Discussion – why GNSS deformation rates should not be directly compared to seismicity and fault-slip rates in the Western Alps

As shown by several studies in the last decade, GNSS velocities and strain rates in the Western Alps are characterized, to a first order, by uplift rates of ca. 1–2 mm yr^{-1} and radial extension rates of ca. 1–3 $\times 10^{-9}$ yr^{-1} (Masson et al., 2019; Nguyen et al., 2016; Nocquet et al., 2016; Sánchez et al., 2018; Walpersdorf et al., 2018). These deformation rates are compatible with the GIA effects from the Last Glacial Maximum, provided the Western Alp region behaves mechanically as a thin elastic plate over a low-viscosity upper mantle (see Sect. 3; Chéry et al., 2016; Mey et al., 2016). Although the exact contribution of GIA relative to other processes (e.g., slab break-off, erosion, tectonics) in the total deformation rates is unclear, the good first-order agreement between GIA model predictions and the observed GNSS rates indicates that the former contributes 30 %–80 % of the latter, at least in the region below the former Würm ice cap (see Sect. 3; Sternai et al., 2019).

The increasing resolution of GNSS horizontal velocities and strain rates has led to direct comparisons of geodetic styles and rates with those of earthquake focal mechanisms. In most cases, these comparisons address the existence or absence of significant aseismic deformation rates captured by GNSS data, with direct implications for the geodynamics of the Western Alps but also eventually the understanding of seismicity and the characterization of the associated seismic hazard. Ultimately, slip rates on specific seismogenic faults can be inferred using standard "plate-boundary" interseismic fault-loading models (Mathey et al., 2020).

Yet, our study shows that, for most faults in the Western Alps, the present-day GIA stress perturbations actually tend to either inhibit fault slip or promote fault slip with the wrong mechanism compared to the seismicity deformation style. Thus, for the present day in the Western Alps, GIA

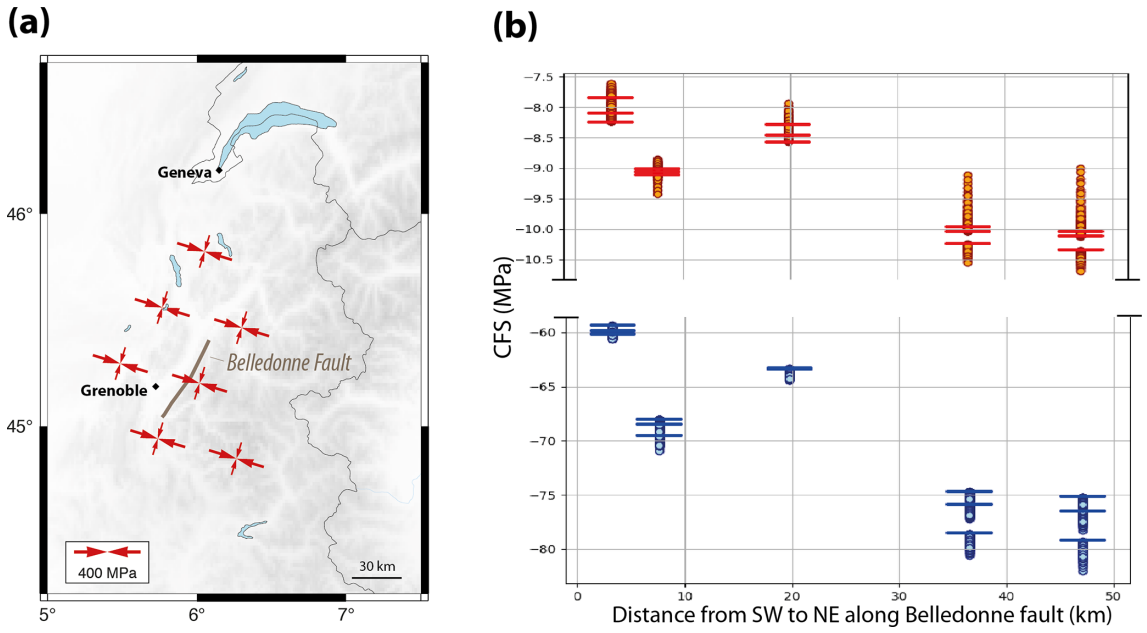

Figure 7. Present-day full stress tensor and Coulomb failure stress (CFS) for the Belledonne Fault system in the northern Western Alps. **(a)** Horizontal full stress (background + GIA) and fault segments tested in the CFS analyses. **(b)** CFS predicted along the Belledonne Fault for three possible fault dips (65, 70, 85°) and 72 GIA models distributed over $5 \leq h_e \leq 40$ km over $3000 \leq \tau_r \leq 7000$ years. Horizontal bars: CFS without GIA perturbation for the three fault dips. Circles: full CFS (background + GIA). Blue and red symbols: $\mu' = 0.6$ and $\mu' = 0.1$.

from the Last Glacial Maximum does not drive or promote the observed seismicity, which must be driven by other processes.

This apparent paradox between GNSS–GIA strain rate agreement and seismicity–GIA stress disagreement is easily resolved by considering that observed GNSS extension rates are merely a diminution over time of the finite shortening induced in the upper crust by its downward flexure under the Würm ice cap. The gradual diminution of the finite shortening (i.e., extensional strain rate) corresponds to the transient return to the pre-ice situation controlled by the upper-mantle relaxation time. This situation bears similarities to that observed in forearcs of subduction zones where finite stress and deformation styles can differ drastically from the transient strain rate patterns observed with GNSS data, the latter being due to the interseismic locking of the subduction fault (Mazzotti et al., 2002; Wang, 2000). A similar situation exists for the early postglacial reverse-faulting earthquakes in Fennoscandia, which occurred during a period of GIA extension strain rates and hence must be the expression of compressive stress stored in the lithosphere over a long (tectonic) time (Craig et al., 2016; Muir-Wood, 2000).

This GIA strain rate–stress antinomy has a major implication for not using GNSS velocities and strain rates in direct comparisons with seismicity styles and rates. Because GIA does not promote the current seismicity, its surface expression, captured in GNSS velocities and strain rates, does not have a simple relationship with seismic-moment rates or fault-slip rates. In other words, GNSS velocities and strain rates comprise a significant part of transient GIA deformation that does not directly contribute to the observed seismicity but rather modulates the expression of the mechanisms (e.g., erosion, slab tear, tectonics) driving the current Western Alp geodynamics and seismicity. In this situation, GNSS data cannot inform models based on a steady-state tectonic process (e.g., far-field fault loading), but they can provide important constraints for models combining long-term forcing and GIA transient to study fault-slip and seismicity variations during and after glaciations (e.g., Steffen et al., 2014; Hetzel and Hampel, 2005). This requires specific models integrating the complexities of the Alpine ice cap history, of the regional crust and mantle rheology heterogeneities, and of the local fault characteristics.

6 Conclusion

Our analysis shows that GIA from the Würm ice cap explains ca. 30 %–80 % of the present-day uplift rates and horizontal extension rates observed by the GNSS in the Western Alps, in agreement with previous studies (Chéry et al., 2016; Mey et al., 2016; Sternai et al., 2019). Yet, we also show that, for most of the major fault systems, present-day GIA stress perturbations either inhibit fault slip or promote it with the wrong mechanism (compared to the seismicity deformation style). Thus, for the present day in the Western Alps, GIA explains most of the geodetic rates but does not drive or promote the observed seismicity. This apparent strain rate–stress

paradox, resulting from the GIA relaxation and diminution over time of the upper-crust flexure, has strong implications for seismicity and seismic-hazard studies. First, because GNSS velocities and strain rates are mostly comprised of transient GIA deformation that tends to inhibit seismicity, they cannot be directly used to estimate seismic-moment rates or fault-slip rates (as would be done in standard plate-boundary interseismic studies). Second, because GIA stress perturbations are decreasing exponentially with a time constant of ca. 5000 years, their inhibition effects on seismicity are slowly disappearing, which should result in an increase in seismicity over the next thousands of years. Thus, seismic-hazard assessments in the Western Alps must integrate the complexities of Würm GIA, constrained through GNSS data and specific modeling, especially for long earthquake return periods and critical facilities.

Code availability. For this article, we coded a plugin software that uses gFlex code (Wickert, 2016). This code can be found with the following DOI: https://doi.org/10.5281/zenodo.8434592 (Grosset and Mazzotti, 2023).

Data availability. No data sets were used in this article.

Supplement. The supplement related to this article is available online at: https://doi.org/10.5194/se-14-1067-2023-supplement.

Author contributions. JG computed the models. JG, SM and PV interpreted and discussed the results and wrote the article.

Competing interests. The contact author has declared that none of the authors has any competing interests.

Disclaimer. Publisher's note: Copernicus Publications remains neutral with regard to jurisdictional claims in published maps and institutional affiliations.

Acknowledgements. Figures were made with the Generic Mapping Tools (Wessel et al., 2013) and Python 3 software. We thank Thierry Camelbeeck, Yann Klinger and Björn Lund for their reviews of and suggestions for early versions of this paper; Rebekka Steffen for an early discussion about this work; Jürgen Mey for providing his numerical Alpine ice cap model; and Manon Gamelin for her first-year MSc internship during the initiation of this work.

Financial support. This research has been supported by the SIGMA-2 research and development project (grant DEFORM_3D).

Review statement. This paper was edited by Patrice Rey and reviewed by Björn Lund and one anonymous referee.

References

Bagge, M., Klemann, V., Steinberger, B., Latinović, M., and Thomas, M.: Glacial-Isostatic Adjustment Models Using Geodynamically Constrained 3D Earth Structures, Geochem. Geophy. Geosy., 22, e2021GC009853, https://doi.org/10.1029/2021GC009853, 2021.

Baize, S., Cushing, M., Lemeille, F., Gelis, C., Texier, D., Nicoud, G., and Schwenninger, J.-L.: Contribution to the seismic hazard assessment of a slow active fault, the Vuache fault in the southern Molasse basin (France), B. Soc. Geol. Fr., 182, 347–365, https://doi.org/10.2113/gssgfbull.182.4.347, 2011.

Battaglia, M., Murray, M. H., Serpelloni, E., and Bürgmann, R.: The Adriatic region: An independent microplate within the Africa-Eurasia collision zone: THE ADRIATIC REGION, Geophys. Res. Lett., 31, L09605, https://doi.org/10.1029/2004GL019723, 2004.

Bilau, A., Rolland, Y., Schwartz, S., Godeau, N., Guihou, A., Deschamps, P., Brigaud, B., Noret, A., Dumont, T., and Gautheron, C.: Extensional reactivation of the Penninic frontal thrust 3 Myr ago as evidenced by U–Pb dating on calcite in fault zone cataclasite, Solid Earth, 12, 237–251, https://doi.org/10.5194/se-12-237-2021, 2021.

Billant, J., Hippolyte, J.-C., and Bellier, O.: Tectonic and geomorphic analysis of the Belledonne border fault and its extensions, Western Alps, Tectonophysics, 659, 31–52, https://doi.org/10.1016/j.tecto.2015.07.025, 2015.

Bott, M. H. P.: The Mechanics of Oblique Slip Faulting, Geol. Mag., 96, 109–117, 1959.

Brandes, C., Steffen, H., Steffen, R., and Wu, P.: Intraplate seismicity in northern Central Europe is induced by the last glaciation, Geology, 43, 611–614, https://doi.org/10.1130/G36710.1, 2015.

Brockmann, E., Ineichen, D., Marti, U., Schaer, S., and Schlatter, A.: Determination of tectonic movements in the Swiss Alps using GNSS and levelling, in: Geodesy for Planet Earth, vol. 136, edited by: Kenyon, S., Pachino, M., and Marti, U., Berlin, Heidelberg, 689–695, 2012.

Bungum, H. and Eldholm, O.: The conundrums of the postglacial tectonic response of the Fennoscandian and Canadian Shields, Earth-Sci. Rev., 232, 104146, https://doi.org/10.1016/j.earscirev.2022.104146, 2022.

Bungum, H., Olesen, O., Pascal, C., Gibbons, S., Lindholm, C., and VestØl, O.: To what extent is the present seismicity of Norway driven by post-glacial rebound?, J. Geol. Soc. London, 167, 373–384, https://doi.org/10.1144/0016-76492009-009, 2010.

Burov, E. B. and Diament, M.: The effective elastic thickness (Te) of continental lithosphere: what does it really mean?, J. Geophys. Res., 100, 3905–3927, 1995.

Calais, E., Han, J. Y., DeMets, C., and Nocquet, J.-M.: Deformation of the North American plate interior from a decade of continuous GPS measurements, J. Geophys. Res., 111, B06402, https://doi.org/10.1029/2005JB004253, 2006.

Champagnac, J.-D., Molnar, P., Anderson, R. S., Sue, C., and Delacou, B.: Quaternary erosion-induced isostatic

rebound in the western Alps, Geology, 35, 195–198, https://doi.org/10.1130/G23053A.1, 2007.

Chéry, J., Genti, M., and Vernant, P.: Ice cap melting and low-viscosity crustal root explain the narrow geodetic uplift of the Western Alps, Geophys. Res. Lett., 43, 3193–3200, https://doi.org/10.1002/2016GL067821, 2016.

Craig, T. J., Calais, E., Fleitout, L., Bollinger, L., and Scotti, O.: Evidence for the release of long-term tectonic strain stored in continental interiors through intraplate earthquakes, Geophys. Res. Lett., 43, 6826–6836, https://doi.org/10.1002/2016GL069359, 2016.

Cushing, E. M., Bellier, O., Nechtschein, S., Sébrier, M., Lomax, A., Volant, P., Dervin, P., Guignard, P., and Bove, L.: A multidisciplinary study of a slow-slipping fault for seismic hazard assessment: the example of the Middle Durance Fault (SE France), Geophys. J. Int., 172, 1163–1178, https://doi.org/10.1111/j.1365-246X.2007.03683.x, 2007.

Cushing, E. M., Bellier, O., Nechtschein, S., Sébrier, M., Lomax, A., Volant, Ph., Dervin, P., Guignard, P., and Bove, L.: A multidisciplinary study of a slow-slipping fault for seismic hazard assessment: the example of the Middle Durance Fault (SE France), Geophys. J. Int., 172, 1163–1178, https://doi.org/10.1111/j.1365-246X.2007.03683.x, 2008.

D'Agostino, N., Avallone, A., Cheloni, D., D'Anastasio, E., Mantenuto, S., and Selvaggi, G.: Active tectonics of the Adriatic region from GPS and earthquake slip vectors, J. Geophys. Res., 113, B09401, https://doi.org/10.1029/2008JB005860, 2008.

Delacou, B., Sue, C., Champagnac, J.-D., and Burkhard, M.: Present-day geodynamics in the bend of the western and central Alps as constrained by earthquake analysis, Geophys. J. Int., 158, 753–774, https://doi.org/10.1111/j.1365-246X.2004.02320.x, 2004.

Freed, A. M., Herring, T., and Bürgmann, R.: Steady-state laboratory flow laws alone fail to explain postseismic observations, Earth Planet. Sc. Lett., 300, 1–10, https://doi.org/10.1016/j.epsl.2010.10.005, 2010.

Giunchi, C. and Spada, G.: Postglacial rebound in a non-Newtonian spherical Earth, Geophys. Res. Lett., 27, 2065–2068, https://doi.org/10.1029/2000GL011460, 2000.

Grellet, B., Combes, P., Granier, T., and Philip, H.: Sismotectonique de la France métropolitaine dans son cadre géologique et géophysique, map number: no. 164 Société Géologique France, 1993.

Grosset, J. and Mazzotti, S.: Software gFlex_load_SE for Glacial Isostatic Adjustment impact on Western Alps, Zenodo [code], https://doi.org/10.5281/zenodo.8434592, 2023.

Hetzel, R. and Hampel, A.: Slip rate variations on normal faults during glacial–interglacial changes in surface loads, Nature, 435, 81–84, 2005.

Hyndman, R. D., Currie, C. A., Mazzotti, S., and Frederiksen, A.: Temperature control of continental lithosphere elastic thickness, Te vs Vs, Earth Planet. Sc. Lett., 277, 539–548, https://doi.org/10.1016/j.epsl.2008.11.023, 2009.

Ivy-Ochs, S., Kerschner, H., Reuther, A., Preusser, F., Heine, K., Maisch, M., Kubik, P. W., and Schlüchter, C.: Chronology of the last glacial cycle in the European Alps, J. Quaternary Sci., 23, 559–573, https://doi.org/10.1002/jqs.1202, 2008.

Jaeger, J. C. and Cook, N. G. W.: Fundamentals of Rock Mechanics, Chapman and Hall., Cambridge University Press, London, 593 pp., ISBN 9781444308914, 1979.

Johnston, A. C.: Suppression of earthquakes by large continental ice sheets, Nature, 330, 467–469, 1987.

Jomard, H., Cushing, E. M., Palumbo, L., Baize, S., David, C., and Chartier, T.: Transposing an active fault database into a seismic hazard fault model for nuclear facilities – Part 1: Building a database of potentially active faults (BDFA) for metropolitan France, Nat. Hazards Earth Syst. Sci., 17, 1573–1584, https://doi.org/10.5194/nhess-17-1573-2017, 2017.

Keiding, M., Kreemer, C., Lindholm, C. D., Gradmann, S., Olesen, O., and Kierulf, H. P.: A comparison of strain rates and seismicity for Fennoscandia: depth dependency of deformation from glacial isostatic adjustment, Geophys. J. Int., 202, 1021–1028, https://doi.org/10.1093/gji/ggv207, 2015.

King, G. C. P., Stein, R. S., and Lin, J.: Static Stress Changes and the Triggering of Earthquakes, B. Seismol. Soc. Am., 84, 935–953, 1994.

Klemann, V. and Wolf, D.: Implications of a ductile crustal layer for the deformation caused by the Fennoscandian ice sheet, Geophys. J. Int., 139, 216–226, https://doi.org/10.1046/j.1365-246X.1999.00936.x, 1999.

Kreemer, C., Blewitt, G., and Davis, P. M.: Geodetic evidence for a buoyant mantle plume beneath the Eifel volcanic area, NW Europe, Geophys. J. Int., 222, 1316–1332, https://doi.org/10.1093/gji/ggaa227, 2020.

Larroque, C., Baize, S., Albaric, J., Jomard, H., Trévisan, J., Godano, M., Cushing, M., Deschamps, A., Sue, C., Delouis, B., Potin, B., Courboulex, F., Régnier, M., Rivet, D., Brunel, D., Chèze, J., Martin, X., Maron, C., and Peix, F.: Seismotectonics of southeast France: from the Jura mountains to Corsica, C. R. Geosci., 353, 105–151, https://doi.org/10.5802/crgeos.69, 2021.

Lau, H. C. P., Austermann, J., Holtzman, B. K., Havlin, C., Lloyd, A. J., Book, C., and Hopper, E.: Frequency Dependent Mantle Viscoelasticity via the Complex Viscosity: Cases From Antarctica, J. Geophys. Res.-Sol. Ea., 126, e2021JB022622, https://doi.org/10.1029/2021JB022622, 2021.

Lund, B.: Palaeoseismology of Glaciated Terrain, in: Encyclopedia of Earthquake Engineering, edited by: Beer, M., Kougioumtzoglou, I. A., Patelli, E., and Au, I. S.-K., Springer Berlin Heidelberg, Berlin, Heidelberg, 1–16, https://doi.org/10.1007/978-3-642-36197-5_25-1, 2015.

Manchuel, K., Traversa, P., Baumont, D., Cara, M., Nayman, E., and Durouchoux, C.: The French seismic CATalogue (FCAT-17), Bull. Earthquake Eng., 16, 2227–2251, https://doi.org/10.1007/s10518-017-0236-1, 2018.

Masson, C., Mazzotti, S., Vernant, P., and Doerflinger, E.: Extracting small deformation beyond individual station precision from dense Global Navigation Satellite System (GNSS) networks in France and western Europe, Solid Earth, 10, 1905–1920, https://doi.org/10.5194/se-10-1905-2019, 2019.

Mathey, M., Walpersdorf, A., Sue, C., Baize, S., and Deprez, A.: Seismogenic potential of the High Durance Fault constrained by 20 yr of GNSS measurements in the Western European Alps, Geophys. J. Int., 222, 2136–2146, https://doi.org/10.1093/gji/ggaa292, 2020.

Mathey, M., Sue, C., Pagani, C., Baize, S., Walpersdorf, A., Bodin, T., Husson, L., Hannouz, E., and Potin, B.: Present-day geody-

namics of the Western Alps: new insights from earthquake mechanisms, Solid Earth, 12, 1661–1681, https://doi.org/10.5194/se-12-1661-2021, 2021.

Mazzotti, S., Dragert, H., Hyndman, R. D., and Miller, M. M.: GPS deformation in a region of high crustal seismicity: N. Cascadia forearc, Earth Planet. Sc. Lett., 198, 41–48, 2002.

Mazzotti, S., James, T. S., Henton, J. A., and Adams, J.: GPS crustal strain, postglacial rebound, and seismic hazard in eastern North America: The Saint Lawrence valley example, J. Geophys. Res., 110, B11301, https://doi.org/10.1029/2004JB003590, 2005.

Mazzotti, S., Aubagnac, C., Bollinger, L., Coca Oscanoa, K., Delouis, B., Do Paco, D., Doubre, C., Godano, M., Jomard, H., Larroque, C., Laurendeau, A., Masson, F., Sylvander, M., and Trilla, A.: FMHex20: A database of earthquake focal mechanisms in metropolitan France and conterminous Western Europe, BSGF – Earth Sciences Bulletin, 192, 10, https://doi.org/10.1051/bsgf/2020049, 2021.

Mey, J., Scherler, D., Wickert, A. D., Egholm, D. L., Tesauro, M., Schildgen, T. F., and Strecker, M. R.: Glacial isostatic uplift of the European Alps, Nat. Commun., 7, 13382, https://doi.org/10.1038/ncomms13382, 2016.

Muir-Wood, R.: Deglaciation Seismotectonics: a principal influence on intraplate seismogenesis at high latitudes, Quaternary Sci. Rev., 19, 1399–1411, 2000.

Nguyen, H. N., Vernant, P., Mazzotti, S., Khazaradze, G., and Asensio, E.: 3-D GPS velocity field and its implications on the present-day post-orogenic deformation of the Western Alps and Pyrenees, Solid Earth, 7, 1349–1363, https://doi.org/10.5194/se-7-1349-2016, 2016.

Nocquet, J.-M., Calais, E., and Parsons, B.: Geodetic constraints on glacial isostatic adjustment in Europe, Geophys. Res. Lett., 32, L06308, https://doi.org/10.1029/2004GL022174, 2005.

Nocquet, J.-M., Sue, C., Walpersdorf, A., Tran, T., Lenôtre, N., Vernant, P., Cushing, M., Jouanne, F., Masson, F., Baize, S., Chéry, J., and van der Beek, P. A.: Present-day uplift of the western Alps, Scientific Reports, 6, 28404, https://doi.org/10.1038/srep28404, 2016.

Peltier, W. R. and Andrews, J. T.: Glacial Isostatic Adjustment I-the Forward Problem, Geophys. J. Roy. Astr. Soc., 46, 605–646, 1976.

Peltier, W. R., Wu, P. P.-C., Argus, D. F., Li, T., and Velay-Vitow, J.: Glacial isostatic adjustment: physical models and observational constraints, Rep. Prog. Phys., 85, 096801, https://doi.org/10.1088/1361-6633/ac805b, 2022.

Qiu, Q., Moore, J. D. P., Barbot, S., Feng, L., and Hill, E. M.: Transient rheology of the Sumatran mantle wedge revealed by a decade of great earthquakes, Nat. Commun., 9, 995, https://doi.org/10.1038/s41467-018-03298-6, 2018.

Quinlan, G.: Postglacial rebound and the focal mechanisms of eastern Canadian earthquakes, Can. J. Earth Sci., 21, 1018–1023, https://doi.org/10.1139/e84-106, 1984.

Rabin, M., Sue, C., Walpersdorf, A., Sakic, P., Albaric, J., and Fores, B.: Present-Day Deformations of the Jura Arc Inferred by GPS Surveying and Earthquake Focal Mechanisms, Tectonics, 37, 3782–3804, https://doi.org/10.1029/2018TC005047, 2018a.

Sánchez, L., Völksen, C., Sokolov, A., Arenz, H., and Seitz, F.: Present-day surface deformation of the Alpine region inferred from geodetic techniques, Earth Syst. Sci. Data, 10, 1503–1526, https://doi.org/10.5194/essd-10-1503-2018, 2018.

Spada, G., Barletta, V. R., Klemann, V., Riva, R. E. M., Martinec, Z., Gasperini, P., Lund, B., Wolf, D., Vermeersen, L. L. A., and King, M. A.: A benchmark study for glacial isostatic adjustment codes, Geophys. J. Int., 185, 106–132, https://doi.org/10.1111/j.1365-246X.2011.04952.x, 2011.

Steffen, H., Kaufmann, G., and Wu, P.: Three-dimensional finite-element modeling of the glacial isostatic adjustment in Fennoscandia, Earth Planet. Sc. Lett., 250, 358–375, https://doi.org/10.1016/j.epsl.2006.08.003, 2006.

Steffen, R., Steffen, H., Wu, P., and Eaton, D. W.: Stress and fault parameters affecting fault slip magnitude and activation time during a glacial cycle, Tectonics, 33, 1461–1476, https://doi.org/10.1002/2013TC003450, 2014.

Steffen, R., Steffen, H., Wu, P., and Eaton, D. W.: Reply to comment by Hampel et al. on "Stress and fault parameters affecting fault slip magnitude and activation time during a glacial cycle", Tectonics, 34, 2359–2366, https://doi.org/10.1002/2015TC003992, 2015.

Steffen, R., Wu, P., and Lund, B.: Geomechanics of Glacially Triggered Faulting, in: Glacially-Triggered Faulting, edited by: Steffen, H., Olesen, O., and Sutinen, R., Cambridge University Press, 20–40, https://doi.org/10.1017/9781108779906.004, 2021.

Stephansson, O.: Ridge push and glacial rebound as rock stress generators in Pennoscandia, Bull. Geol. Inst. U. Uppsala, 14, 39–48, 1988.

Sternai, P., Sue, C., Husson, L., Serpelloni, E., Becker, T. W., Willett, S. D., Faccenna, C., Di Giulio, A., Spada, G., Jolivet, L., Valla, P., Petit, C., Nocquet, J.-M., Walpersdorf, A., and Castelltort, S.: Present-day uplift of the European Alps: Evaluating mechanisms and models of their relative contributions, Earth-Sci. Rev., 190, 589–604, https://doi.org/10.1016/j.earscirev.2019.01.005, 2019.

Stewart, I. S., Sauber, J., and Rose, J.: Glacio-seismotectonics: ice sheets, crustal deformation and seismicity, Quaternary Sci. Rev., 19, 1367–1389, https://doi.org/10.1016/S0277-3791(00)00094-9, 2000.

Stocchi, P., Spada, G., and Cianetti, S.: Isostatic rebound following the Alpine deglaciation: impact on the sea level variations and vertical movements in the Mediterranean region, Geophys. J. Int., 162, 137–147, https://doi.org/10.1111/j.1365-246X.2005.02653.x, 2005.

Stucchi, M., Rovida, A., Gomez Capera, A. A., Alexandre, P., Camelbeeck, T., Demircioglu, M. B., Gasperini, P., Kouskouna, V., Musson, R. M. W., Radulian, M., Sesetyan, K., Vilanova, S., Baumont, D., Bungum, H., Fäh, D., Lenhardt, W., Makropoulos, K., Martinez Solares, J. M., Scotti, O., Živčić, M., Albini, P., Batllo, J., Papaioannou, C., Tatevossian, R., Locati, M., Meletti, C., Viganò, D., and Giardini, D.: The SHARE European Earthquake Catalogue (SHEEC) 1000–1899, J. Seismol., 17, 523–544, https://doi.org/10.1007/s10950-012-9335-2, 2013.

Sue, C. and Tricart, P.: Late Alpine brittle extension above the Frontal Pennine Thrust near Briançon, Western Alps, E-Periodica, Eclogae Geol. Helv., 92, 171–181, 1999.

Sue, C. and Tricart, P.: Neogene to ongoing normal faulting in the inner western Alps: A major evolution of the late alpine tectonics, Tectonics, 22, 1050, https://doi.org/10.1029/2002TC001426, 2003.

Sue, C., Thouvenot, F., Fréchet, J., and Tricart, P.: Widespread extension in the core of the western Alps revealed by earth-

quake analysis, J. Geophys. Res.-Sol. Ea., 104, 25611–25622, https://doi.org/10.1029/1999JB900249, 1999.

Sue, C., Delacou, B., Champagnac, J. D., and Burkhard, M.: Quantification of the seismic strain in the western Alps, in: AGU – EUG Joint Assembly, Abstracts from the meeting held in Nice, France, 6–11 April 2003, abstract ID 10241, https://ui.adsabs.harvard.edu/abs/2003EAEJA....10241S/abstract (last access: October 2023), 2003.

Tarayoun, A., Mazzotti, S., Craymer, M. R., and Henton, J. A.: Structural Inheritance Control on Intraplate Present-Day Deformation: GPS Strain Rate Variations in the Saint Lawrence Valley, Eastern Canada, J. Geophys. Res., 123, 7004–7020, https://doi.org/10.1029/2017JB015417, 2018.

Tesauro, M., Kaban, M. K., and Cloetingh, S. A. P. L.: How rigid is Europe's lithosphere?, Geophys. Res. Lett., 36, L16303, https://doi.org/10.1029/2009GL039229, 2009.

Thouvenot, F., Fréchet, J., Tapponnier, P., Thomas, J.-C., Le Brun, B., Ménard, G., Lacassin, R., Jenatton, L., Grasso, J.-R., Coutant, O., Paul, A., and Hatzfeld, D.: The ML 5.3 Epagny (French Alps) earthquake of 1996 July 15: A long-awaited event on the Vuache Fault, Geophys. J. Int., 135, 876–892, 1998.

Thouvenot, F., Fréchet, J., Jenatton, L., and Gamond, J.-F.: The Belledonne Border Fault: identification of an active seismic strike-slip fault in the western Alps, Geophys. J. Int., 155, 174–192, https://doi.org/10.1046/j.1365-246X.2003.02033.x, 2003.

Turcotte, D. L. and Schubert, G.: Geodynamics, Cambridge University Press, ISBN 978-1-107-00653-9, 978-0-521-18623-0, 2002.

van der Wal, W., Barnhoorn, A., Stocchi, P., Gradmann, S., Wu, P., Drury, M., and Vermeersen, B.: Glacial isostatic adjustment model with composite 3-D Earth rheology for Fennoscandia, Geophys. J. Int., 194, 61–77, https://doi.org/10.1093/gji/ggt099, 2013.

Vernant, P., Hivert, F., Chéry, J., Steer, P., Cattin, R., and Rigo, A.: Erosion-induced isostatic rebound triggers extension in low convergent mountain ranges, Geology, 41, 467–470, https://doi.org/10.1130/G33942.1, 2013.

Walpersdorf, A., Pinget, L., Vernant, P., Sue, C., Deprez, A., and the RENAG team: Does Long-Term GPS in the Western Alps Finally Confirm Earthquake Mechanisms?, Tectonics, 91, 937, https://doi.org/10.1029/2018TC005054, 2018.

Wang, K.: Stress–strain 'paradox', plate coupling, and forearc seismicity at the Cascadia and Nankai subduction zones, Tectonophysics, 319, 321–338, https://doi.org/10.1016/S0040-1951(99)00301-7, 2000.

Wessel, P., Smith, W. H. F., Scharroo, R., Luis, J., and Wobbe, F.: Generic Mapping Tools: Improved Version Released, Eos, Transactions American Geophysical Union, 94, 409–410, https://doi.org/10.1002/2013EO450001, 2013.

Wickert, A. D.: Open-source modular solutions for flexural isostasy: gFlex v1.0, Geosci. Model Dev., 9, 997–1017, https://doi.org/10.5194/gmd-9-997-2016, 2016.

Wu, P.: Viscoelastic versus viscous deformation and the advection of pre-stress, Geophys. J. Int., 108, 136–142, https://doi.org/10.1111/j.1365-246X.1992.tb00844.x, 1992.

Wu, P.: Effects of lateral variations in lithospheric thickness and mantle viscosity on glacially induced surface motion in Laurentia, Earth Planet. Sc. Lett., 235, 549–563, https://doi.org/10.1016/j.epsl.2005.04.038, 2005.

Wu, P. and Mazzotti, S.: Effects of a lithospheric weak zone on postglacial seismotectonics in eastern Canada and the northeastern United States, Geol. S. Am. S., 425, 113–128, https://doi.org/10.1130/2007.2425(09), 2007.

Wu, P., Johnston, P., and Lambeck, K.: Postglacial rebound and fault instability in Fennoscandia, Geophys. J. Int., 139, 657–670, 1999.